Intercalibrated Passive Microwave Rain Products from the Unified Microwave Ocean Retrieval Algorithm (UMORA)

K. A. HILBURN AND F. J. WENTZ

Remote Sensing Systems, Santa Rosa, California

(Manuscript received 1 November 2006, in final form 12 July 2007)

ABSTRACT

The Unified Microwave Ocean Retrieval Algorithm (UMORA) simultaneously retrieves sea surface temperature, surface wind speed, columnar water vapor, columnar cloud water, and surface rain rate from a variety of passive microwave radiometers including the Special Sensor Microwave Imager (SSM/I), the Tropical Rainfall Measuring Mission (TRMM) Microwave Imager (TMI), and the Advanced Microwave Scanning Radiometer for Earth Observing System (AMSR-E). The rain component of UMORA explicitly parameterizes the three physical processes governing passive microwave rain retrievals: the beamfilling effect, cloud and rainwater partitioning, and effective rain layer thickness. Rain retrievals from the previous version of UMORA disagreed among different sensors and were too high in the tropics. These issues have been fixed with more realistic rain column heights and proper modeling of saturation and footprint-resolution effects in the beamfilling correction. The purpose of this paper is to describe the rain algorithm and its recent improvements and to compare UMORA retrievals with Goddard Profiling Algorithm (GPROF) and Global Precipitation Climatology Project (GPCP) rain rates. On average, TMI retrievals from UMORA agree well with GPROF; however, large differences become apparent when the instantaneous retrievals are compared on a pixel-to-pixel basis. The differences are due to fundamental algorithm differences. For example, UMORA generally retrieves higher total liquid water, but GPROF retrieves a higher surface rain rate for a given amount of total liquid water because of differences in microphysical assumptions. Comparison of UMORA SSM/I retrievals with GPCP shows similar spatial patterns, but GPCP has higher global averages because of greater amounts of precipitation in the extratropics. UMORA and GPCP have similar linear trends over the period 1988–2005 with similar spatial patterns.

1. Introduction

The Unified Microwave Ocean Retrieval Algorithm (UMORA) simultaneously retrieves sea surface temperature, surface wind speed, columnar water vapor, columnar cloud water, and surface rain rate from a variety of passive microwave sensors including Special Sensor Microwave Imager (SSM/I), Tropical Rainfall Measuring Mission (TRMM) Microwave Imager (TMI), and the Advanced Microwave Scanning Radiometer (AMSR) (Wentz 1997; Wentz and Spencer 1998; Wentz and Meissner 2000). The products are available on quarter-degree grids in easy-to-use binary file formats with complete documentation and read code at our Web site (http://www.remss.com). The rain retrieval component of the algorithm was developed by Wentz and Spencer (1998, hereinafter WS98). The physical basis for the algorithm is that dual-polarization passive microwave measurements provide an accurate estimate of τ^2—the two-way transmittance through the atmosphere. The three physical processes governing the retrieval of surface rain rate from τ^2 are 1) varying rain intensities across the radiometer footprint (the "beamfilling effect"); 2) the relative partitioning of cloud and rainwater, which depends in part upon the rain drop size distribution; and 3) the effective rain layer thickness ("effective" because of the nonuniform vertical distribution of rainwater). UMORA isolates these processes so it is possible to change them and assess their impact on retrieved rain rates. Thus, we can find physical explanations for discrepancies in our retrievals.

In addition to the retrieval algorithm, the other critical component to obtaining accurate rain retrievals is the radiometer calibration at the brightness temperature (T_B) level. Remote Sensing Systems (RSS) has spent much effort intercalibrating satellite microwave

Corresponding author address: Kyle Hilburn, Remote Sensing Systems, 438 First Street, Suite 200, Santa Rosa, CA 95401.
E-mail: hilburn@remss.com

DOI: 10.1175/2007JAMC1635.1

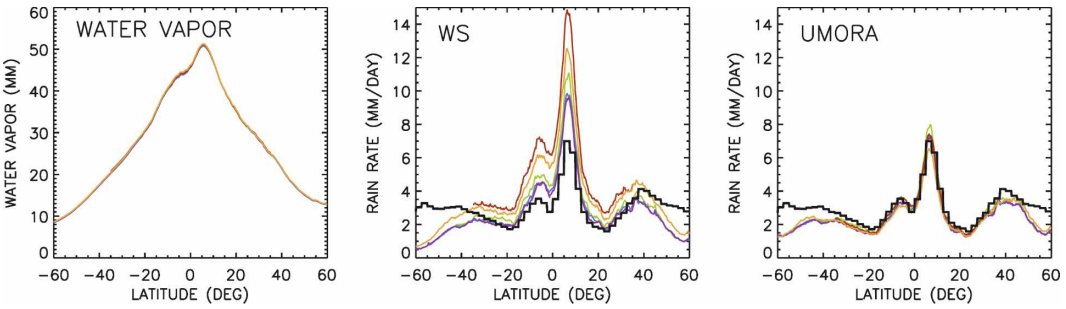

FIG. 1. (left) Zonal average water vapor, (middle) Wentz and Spencer rain rates, and (right) UMORA rain rates for the year 2003. Shown are data from *F13* (green), *F14* (blue), *F15* (purple), AMSR-E (orange), and TMI (dark red). GPCP rain rates are shown for reference (black). Only ocean pixels are considered.

radiometers, starting with SSM/I in 1987. In the most recent version 6, the six SSM/Is have been carefully intercalibrated to a precision of about 0.1 K in T_B, and TMI and the AMSR for Earth Observing System (EOS) (AMSR-E) have been adjusted to match the SSM/I time series. The success of this intercalibration effort can be seen in the excellent agreement of columnar water vapor retrievals shown in Fig. 1. Also, trends in the SSM/I wind speed retrievals now agree with buoy trends to an accuracy of 0.1 m s^{-1} decade^{-1}. Wind speed retrievals are very sensitive to T_B calibration errors, and the good agreement with buoys indicates an intercalibration error of 0.1–0.2 K or less.

Despite the good T_B calibration, the rain retrievals from different sensors did not agree (Fig. 1). The WS98 rain-rate retrievals had two major problems: 1) the rain rates were too high in the tropics and 2) the retrievals from different sensors did not agree. The first problem was due to the use of inappropriate rain column heights. The second problem was due to the failure to include the different resolutions of the sensors (Table 1) in the beamfilling correction. The purpose of this paper is to communicate what has been found in solving these two problems. The answers are not just specific to our algorithm, but have broader applicability to passive microwave rain retrievals. It turns out that other passive microwave rain retrieval algorithms also have intersatellite differences, and removing these artifacts is a major goal of the Global Precipitation Measurement (GPM) mission.

There are two motivations for this paper. The first is to explain the improvements we have made to the WS98 rain algorithm focusing especially on those that address the intersatellite differences. The second motivation is to compare our rain products against other rain products. The goal of this comparison is not to assert that one product is necessarily better than another; but to 1) assess the level of agreement/disagreement that exists and any patterns in the disagreement, 2) examine the microphysical assumptions in our algorithm in comparison with other algorithms to see what role they play in retrieval differences, and 3) to assess long-term trends in the various datasets and compare their consistency. In section 2, we describe the UMORA datasets and the other datasets that we used in this study. In section 3, we describe the rain algorithm and explain changes made to beamfilling (section 3a), cloud and rain partitioning (section 3b), and effective rain layer thickness (section 3c). In section 4 we compare TMI retrievals from UMORA and GPROF to assess their agreement both on average and for instantaneous pixel-to-pixel comparisons. We also examine the consistency of UMORA SSM/I rain retrievals and assess the impact of the diurnal cycle on different SSM/I. Finally, we compare means and trends in UMORA SSM/I rain retrievals with GPCP rain rates.

2. Data

We have intercalibrated the SSM/I (*F08*, *F10*, *F11*, *F13*, *F14*, and *F15*), TMI, and AMSR-E instruments and processed the data with the improved UMORA algorithm. The new data are: version 6 SSM/I, version 4 TMI, and version 5 AMSR-E. The SSM/I provide daily global coverage from July 1987 to the present, TMI provides daily tropical coverage from December 1998

TABLE 1. The geometric average 3-dB footprint sizes for the channels used by the UMORA rain algorithm for SSM/I, TMI (pre/post boost), and AMSR-E.

Sensor	Frequency (GHz)	Avg footprint size (km)
SSM/I	19.35	56
	37.0	32
TMI	19.35	24/28
	37.0	13/15
AMSR-E	18.7	21
	36.5	12

to the present, and AMSR-E provides daily global coverage from June 2002 to the present. Retrievals are done only over the ocean.

Our comparison data include the version 2 Global Precipitation Climatology Project (GPCP) rain rates (Adler et al. 2003) and both the swath level (2A12) and gridded (3A12) version 6 Goddard Profiling Algorithm (GPROF) surface rain rates (Kummerow et al. 2001). The comparison of our TMI swath data with the GPROF swath data is unique because it is a pixel-to-pixel matchup between retrievals from the same sensor on the same satellite. Thus, the differences we find should be almost entirely due to differences between the UMORA and GPROF rain algorithms. It should be noted that we have performed our own independent calibration of TMI (Wentz et al. 2001); however, this should be a small source of discrepancy between UMORA and GRPOF rain rates.

We used several sources of data in our estimation of the effective rain layer thickness. We used the radiosonde dataset described in Wentz (1997) and WS98. We also make use of the National Centers for Environmental Prediction (NCEP) Global Data Assimilation System (GDAS) 0° isotherm height analysis. Our climatological SST product is the National Oceanic and Atmospheric Administration (NOAA)/NCEP Reynolds optimal interpolation (OI) version 2 SST (Reynolds et al. 2002). We also compared our heights with the International Telecommunication Union recommended rain heights (International Telecommunication Union 2001).

3. Algorithm

The brightness temperature at the top of the atmosphere as seen by a satellite radiometer is expressed as the sum of the upwelling atmospheric radiation, downwelling atmospheric radiation that is reflected upward by the sea surface, and the direct emission of the sea surface attenuated by the intervening atmosphere. This can be expressed as follows:

$$F = T_{\mathrm{BU}} + \tau[ET_S + (1 - E)(\Omega T_{\mathrm{BD}} + \tau T_{\mathrm{BC}})], \quad (1)$$

where T_{BU} and T_{BD} are the upwelling and downwelling atmospheric brightness temperatures and τ is the transmittance through the atmosphere, E is the sea surface emissivity, T_{BC} is the cosmic background radiation temperature of 2.7 K, and Ω accounts for nonspecular reflection. The upwelling and downwelling atmospheric brightness temperatures are expressed in terms of effective air temperatures T_U and T_D, defined by

$$T_U = T_{\mathrm{BU}}/(1 - \tau) \quad \text{and} \quad (2a)$$

$$T_D = T_{\mathrm{BD}}/(1 - \tau). \quad (2b)$$

In the nonraining case, there is no scattering, and these effective air temperatures are parameterized as functions of water vapor V and sea surface temperature T_S [i.e., $T_U = \Psi(V, T_S)$ and $T_D = f(T_U, V)$ as in Wentz (1997)]. In the raining case, scattering and rain-induced variations in air temperature make it necessary to make T_U a retrieved parameter. It is assumed that T_D is closely correlated with T_U so that T_D can be specified as a function of T_U as in WS98. It is also assumed that T_U has the same value for vertical and horizontal polarization. In the absence of scattering, T_U is completely independent of polarization. For moderate to heavy rain, T_B observations show that saturation values for the vertical and horizontal polarization are nearly the same; making the assumption of polarization independence seem reasonable. Thus, the retrieval problem is reduced to solving two equations in two unknowns:

$$T_{\mathrm{BV}} = F_V(T_U, \tau^2) \quad \text{and} \quad (3a)$$

$$T_{\mathrm{BH}} = F_H(T_U, \tau^2). \quad (3b)$$

Thus, the physical basis for UMORA is the use of dual-polarization observations in order to separate the emission signal (embodied by the two-way transmission: τ^2) from the scattering signal (embodied by the effective temperature depression: $\Delta T_U = T_U - \Psi$). Equations (3a) and (3b) are quadratic in τ and linear in T_U and can easily be solved. To solve (3a) and (3b) we use the emissivity E and scattering Ω models developed by Wentz (1997) and updated by Meissner and Wentz (2002, 2004). Values for surface wind speed W and columnar water vapor V used by the emissivity model are retrieved as in WS98. The emissivity model also requires values for sea surface temperature, which come from Reynolds OI version 2 SST (Reynolds et al. 2002); and surface wind direction, which comes from NCEP GDAS. The oxygen and vapor components of τ^2 are factored out following WS98, thereby obtaining just the two-way liquid water transmittance τ_L^2.

Equation (1) is complicated and obscures the essential physics of rain retrieval, so it is instructive to examine a simplified form of (1). If we ignore the small effects of nonspecular reflection and the cosmic microwave background, and if we assume that the ocean–atmosphere system is isothermal with an effective temperature of T_E, then we obtain a highly simplified model for brightness temperature:

$$T_B = T_E(\tau)(1 - \tau^2\rho), \quad (4)$$

where ρ is the reflectivity of the sea surface ($\rho = 1 - E$). The effective temperature varies from the sea surface temperature to the effective temperature of the upwelling atmospheric radiation as the transmission goes from 1 to 0. We see that, through the use of vertical and horizontal polarization measurements, T_E can be eliminated and the two-way transmittance is given by

$$\tau^2 = \frac{T_{\mathrm{BV}} - T_{\mathrm{BH}}}{\rho_H T_{\mathrm{BV}} - \rho_V T_{\mathrm{BH}}}. \tag{5}$$

Examining (5), the solution to a simplified version of (1), we see that the essential physics of UMORA are the same as Petty (1994). The advantage of such an approach is that, as shown by Petty (1994), this technique of separating emission and scattering provides accurate estimates of transmittance even in the presence of strong scattering by ice. Moreover, Spencer et al. (1989) show that ice makes a negligibly small absorption contribution relative to that of liquid. Thus, we can obtain reliable estimates of columnar liquid water (the total cloud plus rainwater) even in the presence of scattering by ice.

This simplified model (5) also helps us see that the basic observable for rain retrievals is τ^2, the footprint-averaged two-way transmittance, where (5) has been evaluated with the footprint-average brightness temperatures. Consider, for example, a scene that has uniform $T_S = 27°\mathrm{C}$, $W = 7\ \mathrm{m\ s^{-1}}$, and $V = 60$ mm for SSM/I conditions (incidence angle θ of 53.4° and a frequency of 19.35 GHz). In this case we have $\rho_V = 0.424$ and $\rho_H = 0.716$. Let us say that one-half of the footprint is rain free with $T_{\mathrm{BV}} = 201$ K and $T_{\mathrm{BH}} = 138$ K. The reader can confirm that this implies $\tau = 0.8589$ and $\tau^2 = 0.7377$. Now let us say that the other one-half of the footprint has heavy rain with $T_{\mathrm{BV}} = 268$ K and $T_{\mathrm{BH}} = 263$ K. These values imply $\tau = 0.2494$ and $\tau^2 = 0.0622$. Since brightness temperatures average in the usual linear way, the whole footprint then has values of $\langle T_{\mathrm{BV}} \rangle = 234.5$ K and $\langle T_{\mathrm{BH}} \rangle = 200.5$ K. The angle brackets $\langle\rangle$ denote averaging over the satellite footprint (i.e., the expectation operator). Substituting these values into (5) gives $\tau(\langle T_B \rangle) = 0.6405$ and $\tau^2(\langle T_B \rangle) = 0.4102$. If instead we average the transmission values, we find that $\langle \tau(T_B) \rangle = 0.5542$ and $\langle \tau^2(T_B) \rangle = 0.4000$. In general, it is true that

$$\langle \tau^2(T_B) \rangle = \tau^2(\langle T_B \rangle), \quad \text{whereas} \tag{6a}$$

$$\langle \tau(T_B) \rangle \neq \tau(\langle T_B \rangle). \tag{6b}$$

These facts are confirmed using the full radiative transfer model (1). This example shows that it is τ^2, not τ, that is the basic observable.

Beamfilling enters the picture when estimating attenuation A from the two-way transmission τ^2. To be explicit,

$$\langle \tau^2 \rangle = \langle e^{tA} \rangle = e^{t\hat{A}} \geq e^{t\langle A \rangle}, \quad \hat{A} \leq \langle A \rangle = A, \tag{7}$$

where $t = -2 \sec\theta$, A is the columnar attenuation, and $\hat{A}$ is the estimate of attenuation ignoring beamfilling [i.e., $\hat{A} = \ln(\tau^2)/t$]. It is worth noting that (7) is simply a specific case of Jensen's inequality and the left-hand side of (7) is equivalent to the moment-generating function of the subpixel attenuation probability distribution function. Our technique for estimating the beamfilling adjustment is described in section 3a.

Once an estimate of the two-way liquid water transmittance τ_L^2 is obtained, there are three physical assumptions needed to retrieve the surface rain rate: the beamfilling adjustment (section 3a), the relative partitioning of cloud and rainwater (section 3b), and the rain column height (section 3c). Please note that UMORA performs the retrieval without using adjacent cell information: there is no smoothing, filtering, or analysis of adjacent cell spatial variability.

It is worth noting that in the current version of UMORA our parameterizations are "global." That is, the same rain drop size distribution, rain–cloud threshold, and beamfilling parameterization are used everywhere with no dependence on geographic location, time of year, time of day, ENSO phase, storm type [e.g., ITCZ–southern Pacific convergence zone (SPCZ) convection, tropical cyclone, extratropical transition, extratropical cyclone], or rain type (e.g., convective or stratiform). The advantage of this simple strategy is that the parameterizations are more tightly constrained (i.e., the global average rain rate is bounded by what is hydrologically possible). It is unrealistic, of course, to use a globally constant value of effective rain layer thickness, and the parameterization must depend upon some geographically and/or seasonally variable parameter. The difficulty is that, while passive microwave observations have a strong liquid water attenuation signal, the information needed to convert total liquid water into surface rain rate does not have a strong microwave signal. Ancillary data can be used to help specify these parameterizations (as in our case for the effective rain layer thickness), but care must be taken that the ancillary data do not introduce any spurious long-term trends.

The goal of this phase of algorithm development was relative calibration of the various radiometer rain retrievals. The next step is an absolute calibration. In the next phase of algorithm development, we plan to examine the additional use of passive microwave scatter-

ing information for rain versus cloud thresholding. Hilburn et al. (2006) have seen that passive microwave scattering information (ΔT_U) may provide information about borderline cloud–rain cases, and in the next phase of algorithm development we will examine whether making the cloud–rain threshold a weak function of scattering information will yield benefits. We will also examine the use of scattering and emission information together for the discrimination of different precipitation types (e.g., convective and stratiform). This would allow us to choose different rain drop size distributions and scale the rain column height for more appropriate values of effective rain layer thickness. We plan to examine storm-scale rain structure (see section 4) and use hydrological balance considerations (Wentz et al. 2007) to better constrain our assumptions. These more complicated changes were not made at this time because of the importance of understanding the intersatellite differences coming from our simple rain algorithm before adding additional complexity to the algorithm.

a. Beamfilling

The first step is to go from two-way liquid water transmittance τ_L^2 to liquid water columnar attenuation A_L. This requires knowledge of the spatial distribution of liquid within the satellite footprint and is referred to as the "beamfilling effect." The desired quantity is the footprint-averaged attenuation

$$A_L = \int A' P(A')\, dA', \tag{8}$$

where $P(A')$ is the probability distribution function for attenuation within the footprint. Instead, the measurement gives the footprint-averaged two-way transmittance

$$\tau_L^2 = \int \exp(-2A' \sec\theta) P(A')\, dA'. \tag{9}$$

If the beamfilling were uniform, $P(A')$ would be the delta function, and integrating (9) yields

$$\tau_L^2 = \exp(-2A_L \sec\theta). \tag{10}$$

The estimate of attenuation ignoring beamfilling is

$$\hat{A}_L = -\frac{\ln(\tau_L)}{\sec\theta}, \tag{11}$$

and $\hat{A}_L$ is called the "observed" attenuation because it is directly related to the fundamental measurement τ^2 as compared to the "true" attenuation, which is denoted by A_L. The beamfilling correction multiplier is then defined as

$$B = \frac{A_L}{\hat{A}_L}. \tag{12}$$

If the beamfilling is nonuniform, then we need to assume some form for the spatial distribution of liquid within the footprint, $P(A')$, in order to calculate τ_L^2. Note that calculating τ_L^2 is equivalent to evaluating the moment-generating function of A'_L at $-2\sec\theta$. If we assume that $P(A')$ follows some two-parameter probability distribution function (WS98 assume a gamma distribution), then the departure of the 19–37-GHz attenuation ratio from the theoretical Mie absorption gives the variability of attenuation in the footprint. Thus, the physical basis for the beamfilling correction is the use dual-frequency information to infer subpixel liquid water spatial variability.

The WS98 beamfilling correction had two problems. The first problem was that it did not explicitly account for the spatial resolution of the satellite observations. We find that the form of $P(A')$ changes systematically as a function of footprint size. WS98 assumed a distribution for $P(A')$ that works well for SSM/I resolutions (Table 1), but it assumes more spatial variability than is really present in the smaller TMI and AMSR-E footprints. Thus the beamfilling overcorrected TMI and AMSR-E. We see that neglecting this resolution dependence in the beamfilling correction results in the rain retrievals from the higher-resolution sensors (AMSR-E and TMI) being biased higher than SSM/I, as is shown by the WS98 results in Fig. 1. We also found that the TMI resampling routine was not working correctly for the TMI maneuvers, causing TMI retrievals to be biased even higher as a function of along-scan position. When this problem was fixed, the AMSR-E and TMI rain rates agreed, but were still high relative to SSM/I because of the WS98 algorithm neglecting footprint-resolution effects. In the latest versions, the same resampling algorithm is now used for SSM/I, TMI, and AMSR-E in order to resample the brightness temperatures to a common set of spatial resolutions specific to the sensor (Ashcroft and Wentz 2000). Thus, we produce level 2 (i.e., swath level) rain rates at the resolution of the 37-GHz footprint of the specific instrument (Table 1); however, all of our publicly available gridded data are provided at 0.25° resolution.

The second problem with the WS98 beamfilling correction was that it did not explicitly model saturation. The correction depends on the ratio of 37–19-GHz attenuations, but the response of the 37-GHz channel saturates for lower rain rates than for 19 GHz, causing

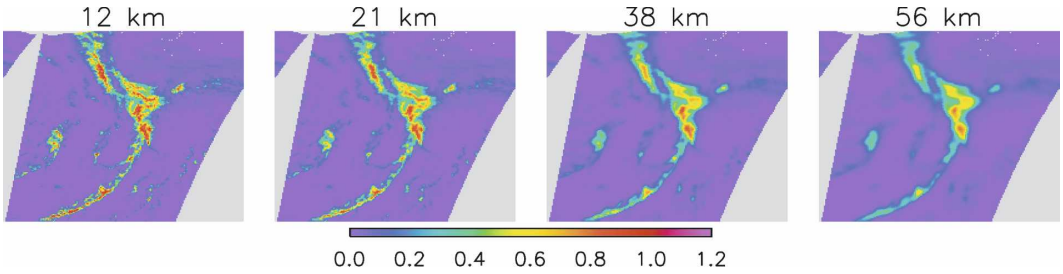

FIG. 2. Attenuation at 37 GHz (nondimensional) is plotted showing an example storm south of the Aleutian Islands on 15 Sep 2003 from our resampled database. Attenuation was retrieved after AMSR-E 37-GHz brightness temperatures were resampled from their original 12-km resolution down to 21-, 38-, and 56-km resolution using optimal interpolation. The scene average attenuations are 1.17, 0.95, 0.86, and 0.79 from left to right. This biasing is known as the beamfilling effect.

spuriously large ratios. Hilburn et al. (2006) found that this caused the WS98 beamfilling correction to reach its maximum allowed values ($B = 3.4$ and 6.4 for the 19- and 37-GHz channels), which produced unrealistic storm structure.

To quantify the saturation and the footprint-resolution effects, we used our optimum interpolation resampling algorithm (Poe 1990; Stogryn 1978; Ashcroft and Wentz 2000) to simulate the effect of beamfilling. The AMSR-E 19- and 37-GHz observations, which have a native resolution of 21 and 12 km, respectively, are resampled down to three spatial resolutions: 21, 38, and 56 km, which are the resolutions of the AMSR-E 19-, 11-, and 7-GHz channels. In doing this we use a month of observations (September 2003). Using the UMORA algorithm, we computed the observed attenuations from (11) for the different spatial resolutions. These results are shown in Fig. 2. Notice that attenuations retrieved from the resampled brightness temperatures are not merely smoothed but are also biased lower. This biasing is known as the beamfilling effect. Figure 2 clearly shows that the magnitude of the beamfilling effect depends on the resolution.

The left panel of Fig. 3 shows the beamfilling multiplier B coming from the AMSR-E simulation. In particular, the 37-GHz beamfilling multiplier for the 56-km resolution is plotted versus $\hat{A}_{19}$ and $\hat{A}_{37}$. For this simulation, the multiplier B is found by setting the true attenuation in (12) to the observed attenuation at the highest AMSR-E resolution of 12 km. Thus, the quantity in Fig. 3 is indicative of the beamfilling effects that occur at the coarser resolution relative to that which occurs at a resolution of 12 km. In essence, the figure represents a beamfilling correction table that is a function of the observables $\hat{A}_{19}$ and $\hat{A}_{37}$. There are similar figures for the other two spatial resolutions (21 and 38 km) and for the 19-GHz beamfilling multiplier, but are not shown.

The middle panel of Fig. 3 shows the beamfilling multiplier B coming from the WS98 algorithm. This algorithm assumes a gamma probability distribution function for $P(A')$, and, referencing the moment-generating function (Hogg and Tanis 1997), it can be shown that the true attenuation A_L is given by

$$A_L = \hat{A}_L\left(\frac{e^{X_{\rm WS}} - 1}{X_{\rm WS}}\right), \tag{13}$$

where $X_{\rm WS} = 2\sec\theta\hat{A}_{\rm L37}\beta^2$, where β is the normalized variance of A'. This value of $X_{\rm WS}$ in (13) produces $A_{\rm L37}$, and it can be shown that multiplying $X_{\rm WS}$ by the ratio $\hat{A}_{\rm L19}/\hat{A}_{\rm L37}$ in (13) produces $A_{\rm L19}$. The WS98 beamfilling correction solved for the value of $X_{\rm WS}$ that produced $A_{\rm L19}$ and $A_{\rm L37}$ matching the theoretical Mie ratio. As can be seen from Fig. 3, this method does not particularly agree well with the simulated results. In particular, for high values of $\hat{A}_{\rm L19}$ and $\hat{A}_{\rm L37}$, the WS98 method gives very large values for B. Also, the WS98 method is solely a function of $\hat{A}_{\rm L19}$ and $\hat{A}_{\rm L37}$ and does not take into account the spatial resolution of the observations.

Through trial and error, we developed an algorithm for finding B that matches the simulation results over a global domain. The three input variables are $\hat{A}_{\rm L19}$, $\hat{A}_{\rm L37}$, and the footprint spatial resolution D. We found that the WS98 method provided a good starting point, and the first step is to compute$X_{\rm WS}$. Then $X_{\rm WS}$ is modified to account for saturation effects and the dependence on D:

$$X = (1 - W)X_{\rm WS} + X_{\rm res}, \tag{14}$$

where W accounts for saturation and $X_{\rm res}$ accounts for departures in $P(A')$ away from a gamma distribution. Saturation is modeled by

$$W = \sqrt{(\hat{A}_{\rm L19}/1.2)^2 + (\hat{A}_{\rm L37}/1.2)^2}, \tag{15}$$

and spatial resolution is modeled by

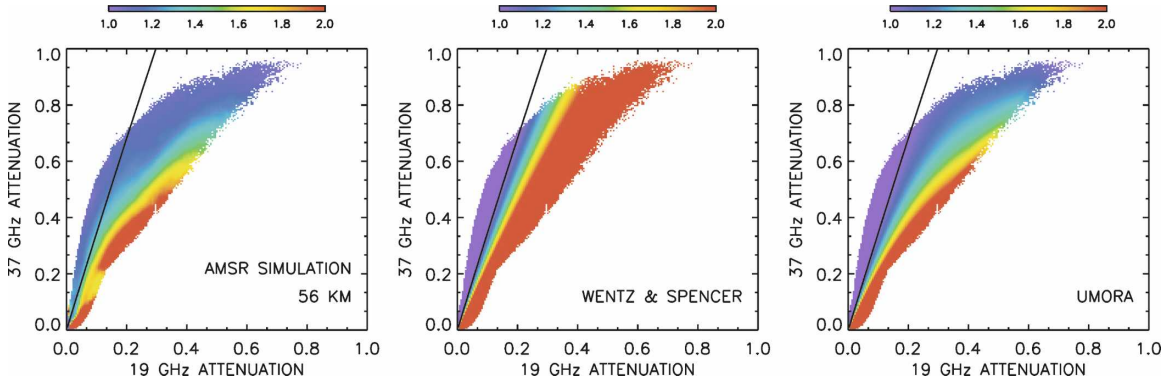

FIG. 3. The multiplicative beamfilling correction factor B for 37 GHz is plotted to contrast (left) the AMSR simulated beamfilling correction, (middle) the WS98 beamfilling correction, and (right) the UMORA beamfilling correction. The theoretical Mie absorption ratio is shown for reference (solid line). Note that in the AMSR simulation as 37-GHz attenuation increases above 0.6, large departures from the theoretical line do not imply large beamfilling correction factors. This is due to saturation, and the UMORA beamfilling correction more accurately models this effect.

$$X_{\text{res}} = \frac{D}{120}, \tag{16}$$

where D is the footprint diameter in kilometers. In the algorithm, we use the value of D associated with the 19-GHz footprint, since that is the footprint size associated with the 19–37-GHz attenuation ratio. The value of X coming from (14) is then substituted into (13) to find the true attenuation. It should be emphasized that (14)–(16) represent an empirical fit to the beamfilling results that come from the AMSR-E simulation. These results represent global coefficients.

The right panel of Fig. 3 shows the new UMORA beamfilling correction. It is clearly more representative of the simulation results. It is small when the attenuations are near the theoretical Mie ratio and increases as the actual ratio departs the Mie ratio. When the attenuation is large, greater than roughly 0.6, the beamfilling correction is small and does not depend as strongly on the 19–37-GHz ratio. This behavior has also been observed by Varma et al. (2004), and is much different than assuming a pure gamma distribution for $P(A')$ (i.e., the WS98 assumption). Figure 4 shows AMSR-E rain rates for a particular storm using both the WS98 and UMORA beamfilling correction. Saturation in the centers of storms caused the WS98 beamfilling correction to produce very high rain rates over unrealistically large areas.

b. Cloud–rain partitioning

The second step in the rain retrieval is to go from columnar liquid water attenuation A_L to columnar cloud L and column-average rain rate R. The basic equations governing this are

$$A_{\text{L19}} = a_{19}(1 - b_{19}\Delta T)L + c_{19}(1 + d_{19}\Delta T)R^{e19}H, \tag{17a}$$

$$A_{\text{L37}} = a_{37}(1 - b_{37}\Delta T)L + c_{37}(1 + d_{37}\Delta T)R^{e37}H, \tag{17b}$$

$$\Delta T = T_L - 283, \quad \text{and} \tag{17b}$$

$$T_L = 251.5 + 0.83(T_U - 240), \tag{17c}$$

where H is the height of the rain column, T_L is the rain cloud temperature, and $T_U = \Psi(V, T_S)$. The values that we use for a, b, c, d, and e are given in Table 2. These coefficients were derived using a Marshall–Palmer rain drop size distribution (see WS98 for more details) and compare well to other accepted standards (e.g., International Telecommunication Union 1999). Note that attenuation is linearly related to the columnar cloud

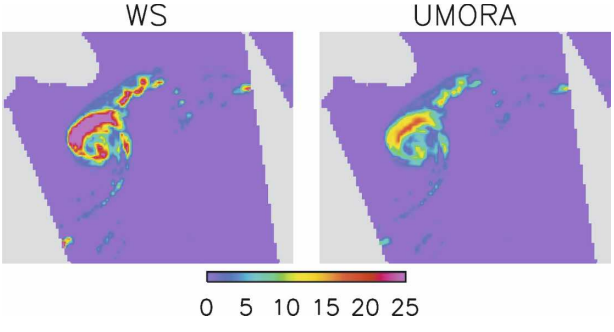

FIG. 4. This storm caught by AMSR-E in the North Atlantic on 7 Sep 2003 is shown to illustrate the impact of properly modeled saturation. Shown are (left) the WS98 rain rates and (right) the UMORA rain rates (mm h^{-1}). Note the changes in the strength of both the center of the storm system and in the isolated showers.

TABLE 2. Coefficients for our cloud and rain attenuation model. The top number is for SSM/I and TMI frequencies and the bottom number is for AMSR-E frequencies.

Frequency	a	b	c	d	e
19 GHz	0.059 48	0.028 71	0.012 21	0.004 00	1.057 10
	0.055 63	0.028 80	0.011 33	0.004 00	1.063 63
37 GHz	0.208 00	0.026 00	0.043 56	−0.002 00	0.951 86
	0.202 71	0.026 08	0.042 49	−0.002 00	0.954 63

water L, and weakly nonlinearly related to the column-average rain rate through the rain drop size distribution. Changes in the drop size distribution will manifest themselves through changes in the cloud and rainwater partitioning. Solving Eqs. (17a) and (17b) requires partitioning the water between cloud and rain. Unfortunately, we have two equations but three unknowns. In addition, if we examine the ratios of the coefficients, we find

$$\frac{a_{19}}{a_{37}} \approx \frac{c_{19}}{c_{37}}, \tag{18a}$$

and

$$e_{19} \approx e_{37} \approx 1. \tag{18b}$$

This means that we cannot use dual-frequency measurements to reliably separate the cloud signal from the rain signal or to estimate rain column height. Thus, while we have only one unique piece of information, we have three unknowns. Based on a study of northeast Pacific extratropical cyclones, WS98 choose a simple partitioning relationship

$$L = \alpha(1 + \sqrt{HR}), \tag{19}$$

where $\alpha = 0.18$ mm. This relationship can be used to solve (17a) and (17b) if we assume some value for H. It is possible that the rain–cloud threshold α might depend on footprint size, and thus could explain discrepancies among sensors. We found that varying α made relatively small changes in the average rain rate, but it made very large changes in the rain coverage (Fig. 5). We concluded that globally adjusting the cloud–rain partitioning threshold to obtain better agreement between the various sensors is a bad option because it resulted in unrealistic rain coverage. We use the WS98 value of 0.18 mm for UMORA. The reasonableness of this value is confirmed (in section 4) by comparing maps of our fractional coverage with maps in Petty (1995).

c. *Effective rain layer thickness*

The third step of the retrieval is to prescribe a value for rain column height H. Doing so, we can solve (17a), (17b), and (19) for the column-average rain rate, which is given by

$$R = H^{-1} \int_0^H R(h)\, dh, \tag{20}$$

where $R(h)$ is the rain profile. The difference between the column-average rain rate R and the surface rain rate $R(0)$ is a source of error when comparing to in situ surface rain measurements. Ideally, we should use the effective rain layer thickness H_{eff} instead of the rain column height. The relationship between the effective rain layer thickness H_{eff} and the rain column height H is given by

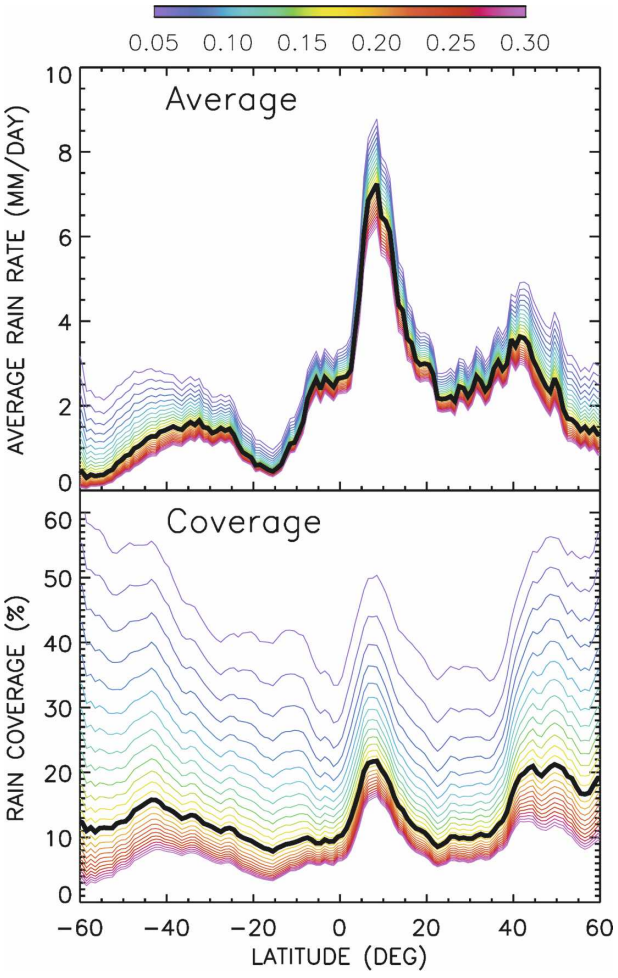

FIG. 5. (top) Zonal average rain rate and (bottom) fractional rain coverage for one month of AMSR-E data where the cloud–rain threshold parameter has been varied from 0.05 to 0.30 mm (color bar). Our algorithm uses a typical value of 0.18 mm (heavy black line) as a threshold. Note that modest changes in average rain rate are associated with large changes in fractional rain coverage.

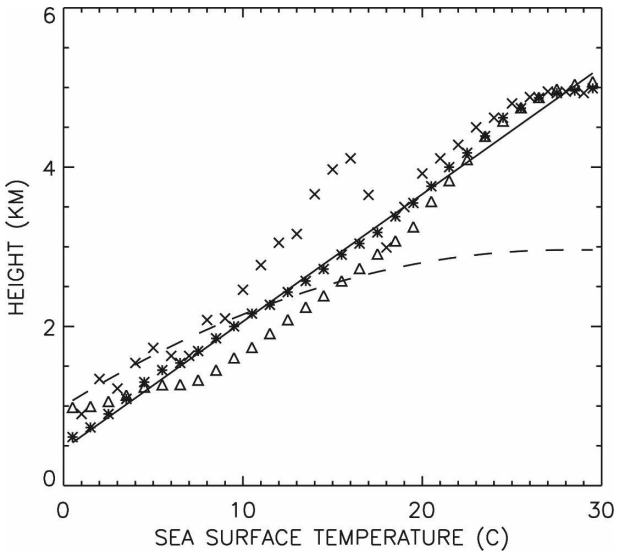

FIG. 6. The WS98 (dashed line) and UMORA (solid line) freezing level heights used by our algorithm are plotted vs climatological SST. Heights from NCEP (asterisk), radiosondes (x), and the ITU (triangle) are shown for reference. The bump in radiosonde heights between 10° and 20°C is because very few observations are available in this temperature range. Only radiosonde observations with surface relative humidity ≥90% and NCEP grid points with integrated cloud water ≥0.18 mm were used in order to make the results more indicative of raining observations.

$$H_{\text{eff}} = H\left[\frac{R}{R(0)}\right]. \tag{21}$$

The present version of UMORA assumes the same value as WS98: $R/R(0) = 1$, but in reality this ratio is a strong function of the microphysical and thermodynamic environment in which the rain is produced (e.g., Liu and Fu 2001). While we recognize that a nonunity value for $R/R(0)$ is probably more physically appropriate, this strong functionality makes it difficult for us to confidently choose a value to be applied globally. Solving (17a) and (17b) produces two estimates of the column-average rain rate, one for the 19-GHz channel and one for the 37-GHz channel. We smoothly blend columnar rain-rate estimates from the 37-GHz channel at low values to the 19-GHz channel at high values.

WS98 used radiosonde observations to derive a relationship between freezing level height and sea surface temperature (SST). They assume the rain column height is the same as the freezing level height. They found that their expression gave rain rates that were about 3/5 smaller than climatology in the tropics. They fixed this discrepancy by forcing the rain column height expression to reach a maximum of 3 km in the tropics; much lower than the 5 km indicated by observations (Fig. 6). They acknowledged that this was a questionable ad hoc correction. We now understand why this correction was required. In computing the average for the tropical rain, the WS98 algorithm excluded observations having very large B. These cases occurred for less than roughly 10% of rain retrievals, and excluding them had a much bigger effect on the average rain rate than WS98 realized. These cases could occur at any rain rate, but formed the majority of rain retrievals greater than 5 mm h^{-1}. Once these cases are included, the average tropical rain increases by 5/3, and there is no need to apply the ad hoc correction to H, and the radiosonde-derived relationship between H and SST can be used as is.

For UMORA, we took a closer look at the H versus SST relationship. We were concerned that the irregular geographic sampling of the radiosonde observations might affect the regression, so we compared the radiosonde observations against NCEP freezing level height (Fig. 6). They agree well in the tropics, disagree somewhat where the radiosonde sampling is most incomplete, and NCEP is slightly lower in the high latitudes. Figure 6 also shows that the International Telecommunication Union (ITU) recommended heights (International Telecommunication Union 2001) agree with NCEP to within 0.5 km. We regressed NCEP freezing level heights against climatological sea surface temperatures, T_{SST}, and found a simple linear relationship fit well:

$$H = 0.46 + 0.16T_{\text{SST}}, \tag{22a}$$

$$H = 0.46, \quad T_{\text{SST}} < 0°\text{C}, \quad \text{and} \tag{22b}$$

$$H = 5.26, \quad T_{\text{SST}} > 30°\text{C}. \tag{22c}$$

This is the relationship now used by UMORA.

4. Comparison

Our comparison consists of two separate activities. The first is to compare TMI rain retrievals from UMORA to GPROF to see how they agree on average, to see how they agree instantaneously, to find reasons for disagreements especially related to microphysical assumptions, and to assess long-term trends. The second activity is to examine SSM/I rain retrievals to see how they agree among themselves, to see what impact the diurnal cycle makes on SSM/I, and to see how well mean and trends over the 18-yr period 1988–2005 compare in the UMORA SSM/I and GPCP datasets.

On average, UMORA and GPROF TMI rain retrievals are very similar. Figure 7 compares average TMI rain rates from UMORA and GPROF for the time period 1998–2005. The UMORA average rain rate tends to be a little higher than GRPOF, except notably

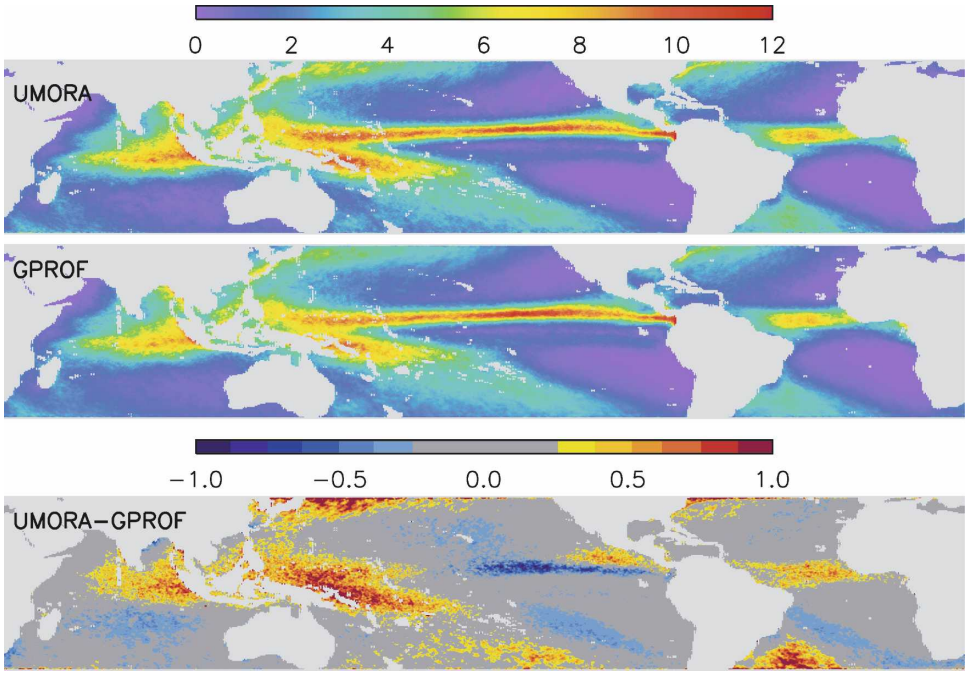

FIG. 7. The 1998–2005 average TMI rain rate for (top) UMORA, (middle) GPROF, and (bottom) the UMORA – GPROF difference (mm day^{-1}). The area-weighted averages are 2.66 mm day^{-1} for UMORA and 2.63 mm day^{-1} for GRPOF with an area-weighted difference of 1.2%.

in the east Pacific. The averages are in good agreement with an overall UMORA–GRPOF area-weighted difference of 1.2%. Figure 8 shows that UMORA and GPROF have very similar patterns of fractional time raining. This is almost surprising considering, as we will see later (Fig. 11), that they have very different cloud–rain partitionings. The differences are that overall UMORA has a consistently slightly higher fractional time raining than GPROF or the climatology of Petty (1995). Since fractional time raining can be sensitive to discretization, the publicly available 0.25° gridded UMORA data are used. Monthly average time series over the tropics of UMORA and GPROF TMI agree to within a steady offset (Fig. 9). Both datasets have a similar annual cycle that dominates the time series. The difference between UMORA and GPROF (0.069 mm day^{-1} on average) is steady through the time period 1998–2005, with no obvious changes after the orbit boost in August 2001. The month-to-month variability (with the annual cycle removed) in both datasets is very similar. Linear trends fit to the time series in Fig. 9 have slopes of +4.4% and +2.7% over the time period 1998–2005 for UMORA and GPROF, respectively.

There are fewer similarities between UMORA and GPROF when instantaneous retrievals are compared on a pixel-to-pixel basis. A joint histogram of UMORA and GRPOF rain rates (Fig. 10) shows that the differences between these retrievals are often quite large. Figure 10 was prepared by matching footprints in the GPROF product with footprints in the UMORA product. Since UMORA performs retrievals at the 37-GHz footprint resolution while GPROF performs retrievals at the 85.5-GHz footprint resolution, UMORA footprints are matched with every other GPROF footprint. The correlation coefficient squared is low: $R^2 = 0.56$. Thinking that the low correlation might be due to differences between UMORA and GPROF in microphysical assumptions, we also examined total liquid water (Fig. 10). The total liquid water is the sum of the vertically integrated precipitation water and the vertically integrated cloud water. Given that the passive microwave technique can accurately estimate the total columnar transmission, and that the transmission is more directly related to the total water than to the surface rain rate; we would expect better agreement between UMORA and GPROF estimates of total liquid water than for surface rain rate. The correlation between total liquid estimates ($R^2 = 0.62$) is not much better than rain rate.

Figure 10 points to more fundamental algorithm differences. Figure 10 shows that UMORA generally retrieves more liquid water than GPROF. This difference indicates either that UMORA has a larger beamfilling correction, or the liquid water profiles in the GPROF retrieval database have much lower values (Fiorino and

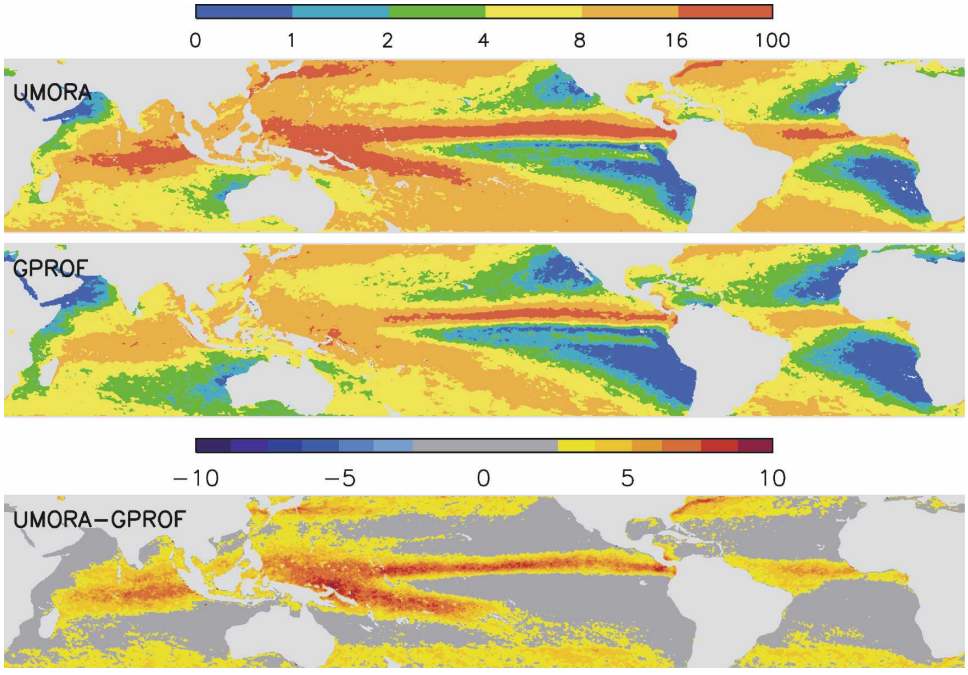

FIG. 8. The fractional time raining (%) during year 2003 from TMI for (top) UMORA, (middle) GPROF, and (bottom) the UMORA – GPROF difference. UMORA has a consistently slightly higher fractional time raining than GPROF or the climatology of Petty (1995).

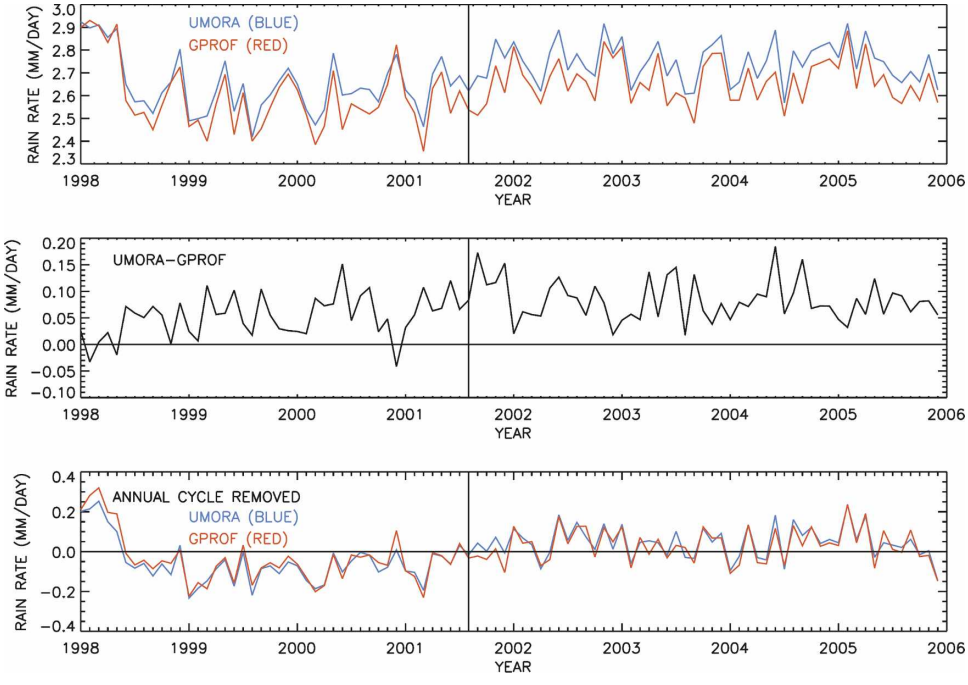

FIG. 9. Monthly time series of TMI retrievals for UMORA and GRPOF for the period 1998–2005. (top) The raw monthly averages show that UMORA (blue line) is consistently slightly higher than GPROF (red line) by 0.069 mm day^{-1} on average. Both datasets have a similar annual cycle. (middle) The monthly average difference UMORA – GPROF shows that the bias is steady in time with no obvious changes after the orbit boost in August 2001 (shown by the black vertical line). (bottom) Removing the annual cycle, it can be seen that UMORA (blue line) and GPROF (red line) have very similar month-to-month variability. Linear trends fit to the time series have slopes of +4.4% and +2.7% over the time period 1998–2005 for UMORA and GPROF, respectively.

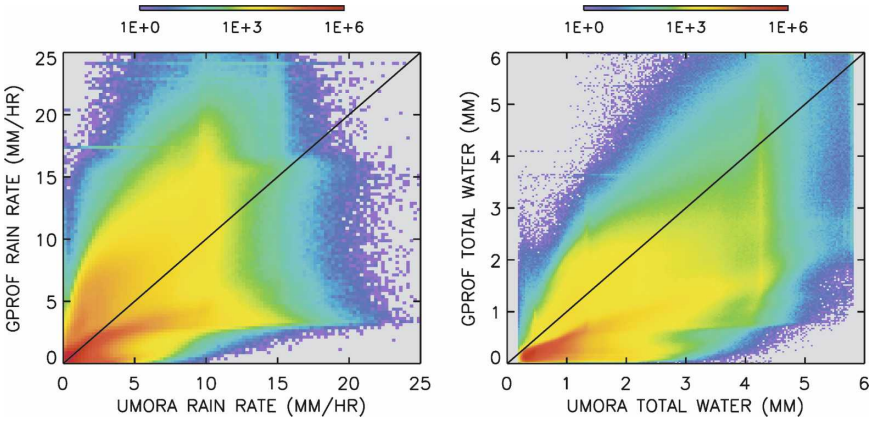

FIG. 10. Colors represent the number of observations in year 2003. (left) The joint histogram of UMORA and GPROF TMI rain rates with a correlation of $R^2 = 0.56$. (right) The joint histogram of UMORA and GPROF TMI total columnar liquid water with a correlation coefficient of $R^2 = 0.62$. The scatter in liquid water estimates is not appreciably better than the scatter in surface rain-rate estimates. UMORA generally retrieves more liquid water than GPROF, but GPROF typically retrieves a greater surface rain rate for a given amount of columnar liquid water. The vertical yellow narrow area around 4.2 mm in the right panel is an artifact of maximum rain rates allowed by the algorithm.

Smith 2006). It is also interesting that, while UMORA generally retrieves much more liquid water, the bias between UMORA and GPROF is small. This is due to the microphysical assumptions regarding cloud and rain partitioning and rain column height. Figure 11 shows that GPROF typically partitions 0.5–1.0 mm less cloud water for a given precipitation water than UMORA. Figure 10 also shows that GPROF surface rain rates are typically larger than the columnar average rain rate. In the GPROF algorithm, the surface rain rate is typically 1.5–1.6 times higher than the column-average rain rate because of the shape of the vertical precipitation water profile. This is in contrast to UMORA, which assumes a constant vertical profile of rain, thus finding a surface rain rate that is equal to the column-average rain rate.

Figure 12 shows tropical storm Ami. We see that in this case UMORA is higher than GPROF in the center of the storm, while GPROF is higher in the rainbands. Informally, we have seen patterns like this in other tropical cyclones. Generally, research on improving microphysical assumptions in rain retrieval algorithms has focused on averages over regional scales. Regional bi-

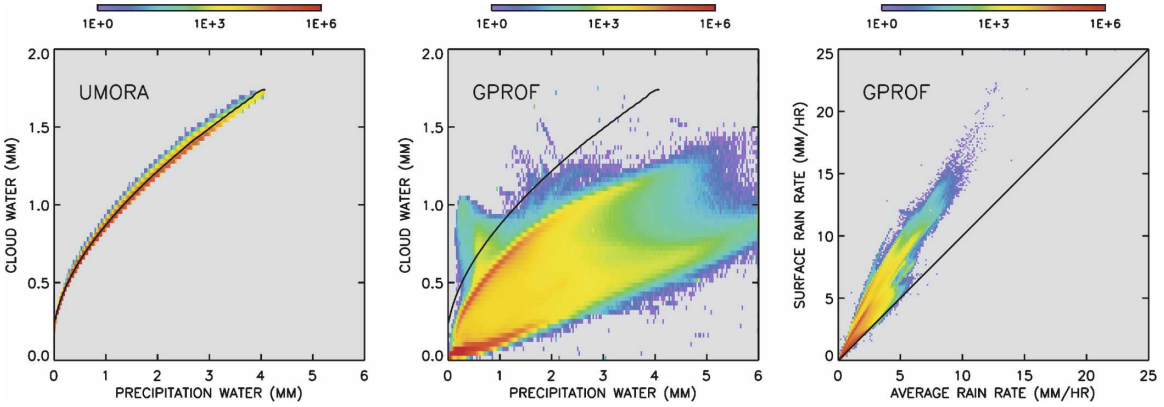

FIG. 11. The colors in each plot represent the number of observations in year 2003. (left) The relationship between cloud water and precipitation water in UMORA is shown. (middle) The relationship for GPROF, where the black line indicates the UMORA relationship, is shown. GPROF partitions more water as precipitation and less as cloud, and there is more scatter between the two parameters. Notice that GPROF can retrieve relatively large amounts of precipitation water with little cloud water. (right) The relationship between surface rain rate and columnar average rain rate in GPROF is shown. The black line is the relationship in UMORA where the surface rain rate is identical to the columnar average rain rate.

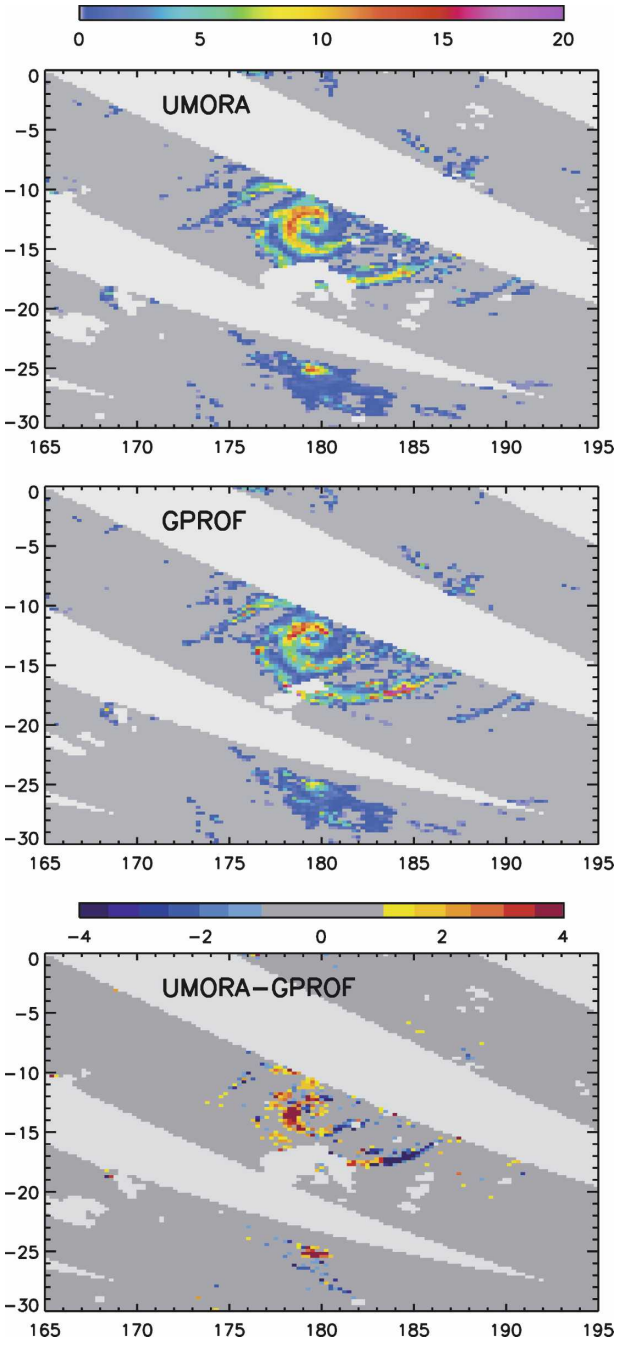

FIG. 12. Tropical Storm Ami at 2000 UTC 12 Jan 2003: (top) UMORA rain rates, (middle) GPROF, and (bottom) the UMORA – GPROF difference (mm h^{-1}). The data have been put on a quarter-degree grid and only data over the ocean are shown. This shows how differences between UMORA and GPROF organize themselves on storm scales. UMORA is higher in the center of the tropical storm and GPROF is higher in the spiral bands.

TABLE 3. The scaling factors to achieve agreement among SSM/I rain rates based on overlap periods. The scaling factors were calculated by matching *F13* to TMI in the tropics, and then working backward in time matching *F15*, *F14*, and *F11* to *F13* globally; *F10* to *F11* globally; and *F08* to *F10* globally. The diurnal scaling factors were derived from the TMI diurnal cycle as shown in Fig. 12. This table shows that much of the discrepancy among various SSM/Is is due to time-of-day effects, with the notable exception of *F10*, which has known instrument problems.

Satellite	Scaling	Diurnal scaling
F08	0.990	0.992
F10	0.908	1.023
F11	0.983	0.994
F13	0.964	0.991
F14	1.015	1.012
F15	1.031	1.024

ases can occur because of differences in the relative proportions of different types of precipitation. Different types of precipitation, however, are also often organized, more fundamentally, on storm scales (e.g., Parker and Johnson 2000). We believe that further understanding and improvements will be made, not so much in analyzing how assumptions affect average values, but in analyzing how changes in assumptions affect storm-scale structure.

To assess UMORA SSM/I rain rates, the first step is to assess the consistency among *F08*, *F10*, *F11*, *F13*, *F14*, and *F15*. This is obviously complicated by the fact that the SSM/I cover different time periods. Also, the SSM/I measure at different local times of day—introducing real geophysical differences. To intercalibrate the rain rates from the different SSM/I sensors for our trend analysis, we apply a scaling factor to rain rate. The scaling factors were calculated by matching *F13* to TMI in the tropics, and then working backward in time matching *F15*, *F14*, and *F11* to *F13* globally, *F10* to *F11* globally, and *F08* to *F10* globally. The resulting scaling factors are shown in the middle column of Table 3. This procedure using overlap periods to remove intersatellite offsets is similar to that done when constructing climate data records from other satellite sensors, such as the Microwave Sounding Unit (Mears et al. 2003). The SSM/I scale factors confirm what our experience with the data has indicated: overall the SSM/I are in good agreement, with the exception of *F10*, which has known sensor and satellite problems. The scaling factors also confirm the general rule that late-morning satellites (such as *F14* and *F15*) tend to have rain rates that are a little low, whereas early-morning satellites (such as *F08*, *F11*, and *F13*) tend to have averages that are a little high. These general rules are suggestive of diurnal biasing.

To further investigate diurnal biasing, we used

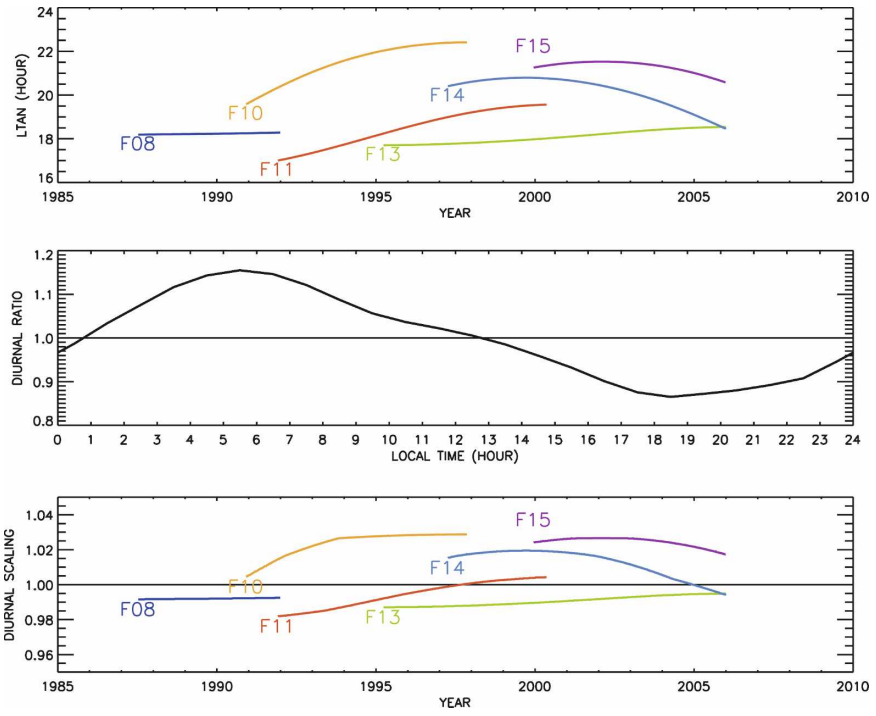

FIG. 13. (top) Local equatorial crossing times of the ascending node for the Defense Meteorological Satellites Program series of SSM/I. Note that *F08* is 12 h out of phase with the other satellites, so the descending node time is plotted. (middle) The ratio of hourly rain to the daily mean based on TMI for 1998–2005. While the cycle had a strong first harmonic, the early-evening trough is slightly flatter than the early-morning peak, thus leading to small systematic biases. (bottom) The diurnal corrections implied by the SSM/I crossing times and the TMI diurnal cycle are shown. Average values are given in the right column of Table 3. Note that in general, late-morning satellites (*F10*, *F14*, and *F15*) have adjustments that increase the average, whereas early-morning satellites (*F08*, *F11*, and *F13*) have adjustments that decrease the average.

UMORA TMI to estimate the impact of the diurnal cycle on SSM/I rain measurements. The diurnal cycle in UMORA TMI rain rates (Fig. 13) match the well-known diurnal cycle of rain over the oceans with an early-morning peak (Imaoka and Spencer 2000). While the diurnal cycle has a strong first harmonic, the morning peak and evening trough have different shapes that produce small biases. Using this diurnal cycle from UMORA TMI and local equatorial crossing times from SSM/I we find that, indeed, early-morning satellites tend to have averages that are a little high (and thus need to be adjusted lower) and late-morning satellites have averages that are a little low (and need to be adjusted higher). Scaling coefficients based on just diurnal effects are given in the rightmost column of Table 3. We have also performed a much more detailed analysis using the actual times for each SSM/I pixel (rather than equatorial crossing times) and find similar behavior. We see that diurnal effects account for much of the difference between various SSM/Is. Except for *F10*, the residual intersatellite bias is less than 3%, which indicates the SSM/I T_B have been well intercalibrated. We might have expected even smaller residual biases given that the over-ocean intercalibration is estimated to be at the 0.1-K level. However, the over-ocean calibration is done for rain-free scenes for which very accurate radiative transfer models are available. The brightness temperatures for moderate to heavy rain can be 100 K warmer than these calibration scenes, and nonlinearity in the radiometer response function or multiplicative errors arising from small errors in spillover or hot load specification may be responsible for the small residual errors. The *F10* SSM/I remains somewhat of a mystery to us, and the exact cause of its calibration problems is an open issue. Please note that none of the correction factors shown in Table 3 are applied to our publicly available data. Once we better understand their physical basis, we will account for them using a more rigorous process.

Having assessed the agreement among SSM/I, we ap-

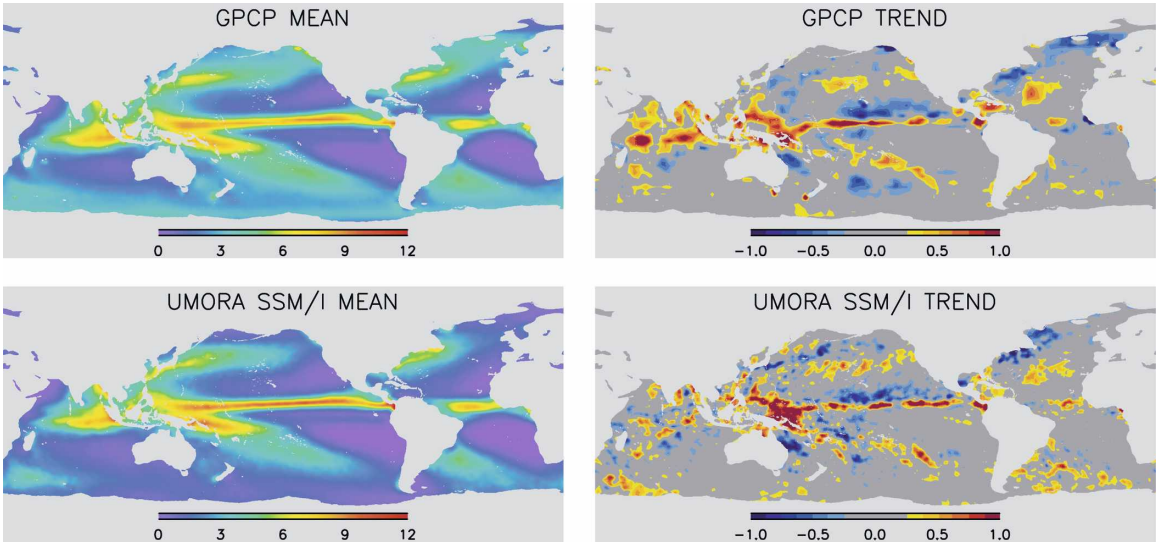

FIG. 14. (top left) The 1988–2005 GPCP mean rain rate and (bottom left) UMORA rain rate from all SSM/I (mm day^{-1}). GPCP has an area-weighted average of 2.99 mm day^{-1} over the ocean during this time period. UMORA has an area-weighted average of 2.46 mm day^{-1}. (top right) The 1988–2005 GPCP linear trend in rain rate and (bottom right) the UMORA rain-rate trend from all SSM/I (mm day^{-1} decade^{-1}). The global average trends are +1.5% and +1.8% decade^{-1} for GPCP and UMORA SSM/I.

ply the scale factors in Table 3 and compare UMORA SSM/I with GPCP. Figure 14 shows that UMORA SSM/I and GPCP agree well in the tropics, but the GPCP dataset has considerably more precipitation in the extratropics. This extra precipitation causes GPCP to be about 20% higher the UMORA SSM/I in the global average. The source of this difference is unclear. It is possible that GPCP retrieves more precipitation in midlatitudes because of its use of infrared satellite data. It is possible that UMORA retrieves less precipitation because it only considers liquid precipitation. Wentz et al. (2007) address this issue from a hydrological balance perspective, and their results suggest that UMORA rain rates may be too low in mid–high latitudes but that the truth cannot be too much higher than GPCP values. This would point to rain column heights that need to be lower in midlatitudes (closer to the ITU values in Fig. 6) or vertical rain profiles that have $R/R(0) < 1$ in midlatitudes (meaning that the surface rain rate is higher than the columnar rain rate). Figure 14 also compares linear trends. Overall, these two datasets have remarkably similar trends, both in spatial pattern and magnitude. Both datasets have roughly a 10% increase in precipitation in the ITCZ and over the western Pacific warm pool. The GPCP has a much stronger increase in the Indian Ocean than UMORA SSM/I. Annual average time series are shown in Fig. 15. After 1997, the time series are remarkably similar, both globally and in the tropics. It is unclear why the datasets differ before 1997. Figure 15 also compares SSM/I versus the SSM/I "backbone," which is calculated using just one SSM/I at a time. That is, the backbone starts with F08 and then switches to *F10* when it is available, then to *F11* when it is available, and finally to *F13* when it is available. Thus, the changing number of SSM/I is not a large source of uncertainty, and SSM/I backbone trend maps (not shown) are very similar to the SSM/I trend map in Fig. 14. Figure 15 also shows that UMORA TMI agrees well with UMORA SSM/I and GPCP in the tropics. The global average trends are +1.5%, +1.8%, and +2.4% decade^{-1} for GPCP, UMORA SSM/I, and the UMORA SSM/I backbone, respectively. The tropical trends are +2.7%, +2.0%, and +3.5% decade^{-1} for GPCP, UMORA SSM/I, and the UMORA SSM/I backbone, respectively. The differences between these trends indicate the sensitive nature of trend analysis.

5. Conclusions

The Unified Microwave Ocean Retrieval Algorithm (UMORA) provides a consistent 18-yr record of simultaneous retrievals of sea surface temperature, wind speed, water vapor, cloud water, and rain rate from SSM/I, TMI, and AMSR-E. Brightness temperatures have been intercalibrated to the 0.1-K level. The rain component of UMORA is an improvement of the WS98 rain algorithm. Several problems with the WS98 algorithm were found (resampling, beamfilling, and rain column height) and were corrected in a physically consistent manner. In particular, the rain column height

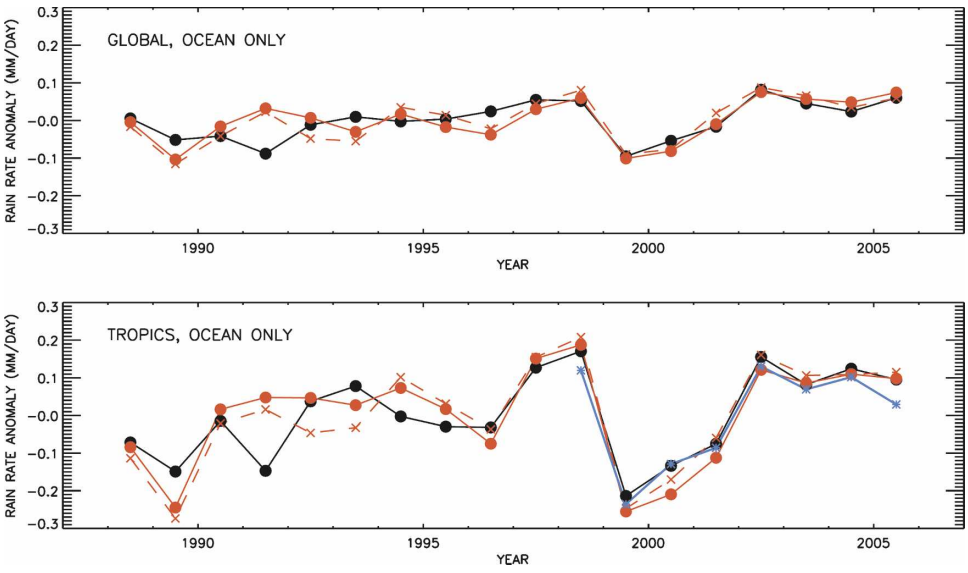

FIG. 15. Time series of annual rain-rate anomalies from the 18-yr (1988–2005) average for GPCP (black dot, solid line), UMORA SSM/I (red dot, solid line), and UMORA SSM/I using just the "backbone" of SSM/I (red x, dashed line) for (top) the global ocean and (bottom) the tropical ocean from 20°N to 20°S. The bottom panel also shows UMORA TMI (blue asterisk, solid line). The SSM/I backbone uses just one SSM/I at a time, starting with *F08*, then switching to *F10* when it becomes available, then to *F11* when it becomes available, and finally to *F13* when it becomes available. The backbone shows that the changing number of SSM/I in the average of all SSM/I is not a significant source of uncertainty in global average time series. Notice that GPCP is well correlated with UMORA after 1997, but the correlation between the time series is lower prior to 1997.

is more realistic and a beamfilling correction is applied that agrees with simulation results. The UMORA beamfilling correction explicitly accounts for radiometer saturation and footprint-resolution effects. Once these corrections are applied, the UMORA rain retrievals are consistent across satellite platform and sensor type. It is shown that much of the small remaining differences among UMORA SSM/I rain retrievals are due to real geophysical time-of-day effects. When diurnal effects are removed, the agreement among the SSM/I, TMI, and AMSR-E rain rates are within ±3%, except for SSM/I *F10*, which has a unique set of calibration problems. The remaining discrepancy may be due to nonlinearity in the calibration equation or multiplicative errors arising from small errors in spillover or hot load specification.

UMORA rain retrievals are in reasonable agreement with other datasets. UMORA TMI retrievals agree very well on average with GPROF TMI retrievals. However, a comparison of instantaneous pixel-to-pixel retrievals showed large differences that are due to different microphysical assumptions. UMORA SSM/I agree well with GPCP in the tropics, however GPCP has greater precipitation in the extratropics. Trends in all of the datasets have similar spatial patterns and agree to within 50% on average. Despite the remaining uncertainties in passive microwave rain retrieval, the overall similarity of trends in the datasets suggests that the rain rates can be used with reasonable confidence for climate studies on time scales of years to decades.

Acknowledgments. We are very grateful for continuing support from the National Aeronautics and Space Administration (NASA). We are thankful to the Defense Meteorological Satellite Program for making the SSM/I data available to the civilian community. We have been supported by NASA NEWS under Contract NNG05OAR4311111 and by DISCOVER, which is supported by the NASA Earth Science Research, Education, and Applications Solution Network (REASoN) Project under Cooperative Agreement NNG04GG46A. REASoN is a distributed network of data and information providers for NASA's Earth Science Enterprise (ESE) Science, Applications, and Education programs. REASoN provides vital links between NASA's data, modeling, and systems engineering capabilities and the user communities in research, applications, and education. The AMSR-E work was partially supported by NASA Contract NNG04HZ47C. We are grateful to three anonymous reviewers whose comments have greatly enhanced the clarity of this paper.

The GPCP combined precipitation data were devel-

oped and computed by the NASA Goddard Space Flight Center's Laboratory for Atmospheres as a contribution to the GEWEX Global Precipitation Climatology Project. GPROF TMI data used in this study were acquired as part of the Tropical Rainfall Measuring Mission (TRMM). The algorithms were developed by the TRMM Science Team. The data were processed by the TRMM Science Data and Information System (TSDIS) and the TRMM Office; they are archived and distributed by the Goddard Distributed Active Archive Center. TRMM is an international project jointly sponsored by the Japan National Space Development Agency (NASDA) and the U.S. NASA Office of Earth Sciences.

REFERENCES

Adler, R. F., and Coauthors, 2003: The version 2 Global Precipitation Climatology Project (GPCP) Monthly Precipitation Analysis (1979–present). *J. Hydrometeor.,* **4,** 1147–1167.

Ashcroft, P., and F. J. Wentz, 2000: Algorithm theoretical basis document: AMSR level 2A algorithm. RSS Tech. Rep. 121599B-1, Remote Sensing Systems, 29 pp.

Fiorino, S. T., and E. A. Smith, 2006: Critical assessment of microphysical assumptions within TRMM radiometer rain profile algorithm using satellite, aircraft, and surface datasets from KWAJEX. *J. Appl. Meteor. Climatol.,* **45,** 754–786.

Hilburn, K. A., F. J. Wentz, D. K. Smith, and P. D. Ashcroft, 2006: Correcting active scatterometer data for the effects of rain using passive radiometer data. *J. Appl. Meteor. Climatol.,* **45,** 382–398.

Hogg, R. A., and E. A. Tanis, 1997: *Probability and Statistical Inference.* 5th ed. Prentice Hall, 722 pp.

Imaoka, K., and R. W. Spencer, 2000: Diurnal variation of precipitation over the tropical oceans observed by TRMM/TMI combined with SSM/I. *J. Climate,* **13,** 4149–4158.

International Telecommunication Union, 1999: Specific attenuation model for rain for use in prediction methods. ITU-R Recommendation P.838, 2 pp.

——, 2001: Rain height model for prediction methods. ITU-R Recommendation P.839, 2 pp.

Kummerow, C., and Coauthors, 2001: The evolution of the Goddard Profiling Algorithm (GPROF) for rainfall estimation from passive microwave sensors. *J. Appl. Meteor.,* **40,** 1801–1820.

Liu, G., and Y. Fu, 2001: The characteristics of tropical precipitation profiles as inferred from satellite radar measurements. *J. Meteor. Soc. Japan,* **79,** 131–143.

Mears, C. A., M. C. Schabel, and F. J. Wentz, 2003: A reanalysis of the MSU channel 2 tropospheric temperature record. *J. Climate,* **16,** 3650–3664.

Meissner, T., and F. J. Wentz, 2002: An updated analysis of the ocean surface wind direction signal in passive microwave brightness temperatures. *IEEE Trans. Geosci. Remote Sens.,* **40,** 1230–1240.

——, and ——, 2004: The complex dielectric constant of pure and sea water from microwave satellite observations. *IEEE Trans. Geosci. Remote Sens.,* **42,** 1836–1849.

Parker, M. D., and R. H. Johnson, 2000: Organizational modes of midlatitude mesoscale convective systems. *Mon. Wea. Rev.,* **128,** 3413–3436.

Petty, G. W., 1994: Physical retrievals of over-ocean rain rate from multichannel microwave imagery. Part I: Theoretical characteristics of normalized polarization and scattering indices. *Meteor. Atmos. Phys.,* **54,** 79–99.

——, 1995: Frequencies and characteristics of global oceanic precipitation from shipboard present-weather reports. *Bull. Amer. Meteor. Soc.,* **76,** 1593–1616.

Poe, G. A., 1990: Optimal interpolation of imaging microwave radiometer data. *IEEE Trans. Geosci. Remote Sens.,* **28,** 800–810.

Reynolds, R. W., N. A. Rayner, T. M. Smith, D. C. Stokes, and W. Wang, 2002: An improved in situ and satellite SST analysis for climate. *J. Climate,* **15,** 1609–1625.

Spencer, R. W., H. M. Goodman, and R. E. Hood, 1989: Precipitation retrieval over land and ocean with the SSM/I: Identification and characteristics of the scattering signal. *J. Atmos. Oceanic Technol.,* **6,** 254–273.

Stogryn, A., 1978: Estimates of brightness temperatures from scanning radiometer data. *IEEE Trans. Antennas Propag.,* **26,** 720–726.

Varma, A. K., G. Liu, and Y.-J. Noh, 2004: Subpixel-scale variability of rainfall and its application to mitigate the beam-filling problem. *J. Geophys. Res.,* **109,** D18210, doi:10.1029/2004JD004968.

Wentz, F. J., 1997: A well-calibrated ocean algorithm for special sensor microwave/imager. *J. Geophys. Res.,* **102,** 8703–8718.

——, and R. W. Spencer, 1998: SSM/I rain retrievals within a unified all-weather algorithm. *J. Atmos. Sci.,* **55,** 1613–1627.

——, and T. Meissner, 2000: AMSR ocean algorithm, version 2. RSS Tech. Rep. 121599A-1, Remote Sensing Systems, 66 pp.

——, P. D. Ashcroft, and C. L. Gentemann, 2001: Post-launch calibration of the TRMM microwave radiometer. *IEEE Trans. Geosci. Remote Sens.,* **39,** 415–422.

——, L. Ricciardulli, K. Hilburn, and C. Mears, 2007: How much more rain will global warming bring? *Science,* **317,** 233–235.